IASS 2020/21 SURREY 7
International Conference on Spatial Structures 2020/21

Proceedings of the IASS Annual Symposium 2020/21 and the 7th International Conference on Spatial Structures
Inspiring the Next Generation
23 – 27 August 2021, Guilford, UK
S.A. Behnejad, G.A.R. Parke and O.A. Samavati (eds.)

Performative Porosity – adaptive infills for architectural elements

Mathias BERNHARD*[,a], Mohammad BOLHASSANI[b], Masoud AKBARZADEH[a,c]

*[,a] Polyhedral Structures Laboratory, Weitzman School of Design, University of Pennsylvania, Philadelphia, PA 19104, USA
mathbern@design.upenn.edu

[b] Bernard and Anne Spitzer School of Architecture, The City College of New York
[c] General Robotic, Automation, Sensing and Perception (GRASP) Lab, School of Engineering and Applied Science, University of Pennsylvania, PA, 19146, USA

Abstract

This research investigates a specific type of porous lattice structures, triply periodic minimal surfaces (TPMS) as potential candidates for infills of architectural elements. It introduces modifiers to manipulate specific parameters of these lattice input geometries, either globally or locally, to control certain performative properties. More specifically, in this investigation, the principal stress distribution obtained through finite element analysis (FEA) or geometry-based form finding method of polyhedral graphic statics is used to guide the infill structures and material. This research takes advantage of the possibilities of additive manufacturing regarding geometric freedom and internal part definition, to design and build lightweight structures. It thereby focuses not on achieving one global maximum for a particular load case only but provides a set of computational design instruments that allow for a variety of design options. The geometry is described as scalar fields in the form of signed distance functions (SDF). The modifiers also come in numerical form, as constants, scalar fields or vector fields, and the modifications are done with pure mathematical operations. The resulting shapes are therefore computed, rather than constructed. This method is more robust for complex Boolean operations and topology changes compared with the more conventional boundary representation of geometry.

Keywords: volumetric modelling, signed distance function, field-driven design, lattices, micro-structures, triply periodic minimal surfaces, finite element analysis, 3D graphic statics, topology optimization

1. Introduction

Advances in digital fabrication methods, especially additive manufacturing (AM) or 3D printing, opened a whole new range of possibilities to many industries. While more conventional subtractive manufacturing methods could only treat the outer boundary of a shape by carving it out of a solid block, AM builds parts up layer by layer. A plethora of different processes, mechanic setups and materials and combinations thereof exist. What they have in common is the increased geometrical degrees of freedom they offer. Parts no longer need to consist of solid material (as they were when milled or cast) but can be detailed throughout the entire volume and made selectively porous. These porosities can be of different types and serve different purposes; depending on the specific production procedure, the resulting structures can be of a high resolution and very filigree. When applied at a nano-meter scale, even the usually brittle material ceramic can be turned into a recoverable, elastic material [1].

1.1. Definition of porosity

Porosity is defined as the ratio between the amount of void (or non-solid) in a total volume of material:

$$\Phi = \frac{V_V}{V_V + V_S} \tag{1}$$

where Φ is the porosity, V_V is the void fraction (e.g. air inclusions) and V_S is the solid fraction that together add up to the total volume. The porosity Φ is therefore a real number between *0* (completely solid) and *1* (completely void). Many different types of porosity exist in natural materials and have been intensively studied [2]. These studies are mainly related to the process by which the substance was formed over time, e.g. by aggregating particles, by solidified inclusions of gas bubbles (foam, tuff), or by selectively growing or shrinking parts of tissue based on structural necessities (bone). Foams are further distinguished into the categories open-cell and closed-cell. The topology of V_V, whether or not the void parts of a material are connected, has a very critical influence on the material's physical properties (e.g. thermal insulation capacity). Natural porous materials range from strongly stochastic (high degree of randomness) to strongly regular (repetitive and predictable). To synthetically produce porosities that reflect this diversity and profit from the opportunities AM offers, algorithmic procedures are needed to geometrically and mathematically describe them in a digital model.

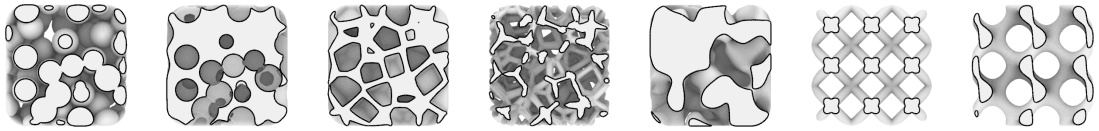

Figure 1: Different types of porosities: (a) aggregate of particles; (b) inverse of a, solid between air bubbles; (c) Voronoi cells (closed foam); (d) Voronoi edges (open foam); (e) cubic noise; (f) truss-based lattice; and (g) triply periodic minimal surface (TPMS).

Semi-random materials can be generated by geometrically simulating their natural counterparts. The samples (a) to (d) in Figure 1 show examples for this type of porosity. The sample (a) results from the Boolean union of randomly distributed spherical particles, (b) is the inverse of (a), the Boolean subtraction of the particles from the total volume, (c) shows a closed-cell foam with solid walls separating the Voronoi cells around the random particle centres and (d) is an open-cell foam with only the common edges between three neighbouring cells from (c) solidified. Porosities can furthermore be modelled with noise functions (Perlin, simplex, cubic, cellular, etc.) as shown in (e), which is a way to reduce entropy in pure randomness, by making local values depending on their neighbouring values. And finally, different families of micro-structures exist to generate regular porosities. The two main families are lattices and triply periodic minimal surfaces (TPMS) [3]. The distinction is that lattices are based on spatial trusses in a unit cell (axis lines thickened with specific cross section profiles), repeated in all three spatial directions. TPMS also repeat in all three spatial directions (hence the name triply periodic) but are – or can be approximated by – trigonometric functions.

The unpredictability in behaviour of porous structures based on random numbers makes them less suitable candidates for parts that have to respond to certain mechanical requirements. The regular lattices are therefore more commonly used for these applications. The functions these porosities have to fulfil, the types and objectives of their performance can again be very different and an attempt at classifying them follows below.

1.2. Definition of performance

Porosities, or the inclusion of void fractions in a solid volume in various forms as described above can have different effects on the behaviour of the part. The most direct outcome is obviously that the part becomes lighter. In return, the same part can become more brittle and withstand fewer external forces. The method part of this paper will focus on how smart geometric configuration of solid and void parts

help maintain structural integrity and performance. But besides structural lightweightness, porosity can fulfil a plethora of alternative functions, some of which are outlined here. The inclusion of immobile air increases the thermal insulation capacity of a part. Cavities connected to the part's surface, especially when in various sizes and proportions, are beneficial for acoustic absorption, while an articulated multifaceted surface affects the diffusive behaviour. Appropriately designed spatial grids in medical implants can foster the tissue growth and better osseointegration by providing a scaffold to encourage cell on- and in-growth into the pore spaces [4]. Compressible layers in sports gear can act as shock absorbent and distribute impact forces to avoid injuries [5]. TPMS introduced in the previous chapter divide the void space into interwoven but non-intersecting volumes, separated by the two-manifold minimal surface. This property makes them ideal candidates for heat exchangers [6,7].

2. Method

We start with regular periodic micro-structures described in the form of signed distance functions (SDF), defining space as a scalar field. We then use modifiers (e.g. constants, other fields) to adjust specific parameters of the base lattice to adjust its properties. In this paper, this generic workflow is illustrated with TPMS as the input lattice and the principal stress concentration as the modifying field. The overview in Figure 1 introduces the ingredients and a vocabulary, that will be used to classify and compare the types of modifications enumerated in section 2.3. The diagram sequence takes a field F_I as its input, a field F_M as modifier, modifies the dimensions D and outputs a new field F_O. We will hence denote this as *(F)(F)(D)(F)*, where each pair of parenthesis stands for one of the categories 1-4 in Figure 1 and can contain arbitrarily many objects.

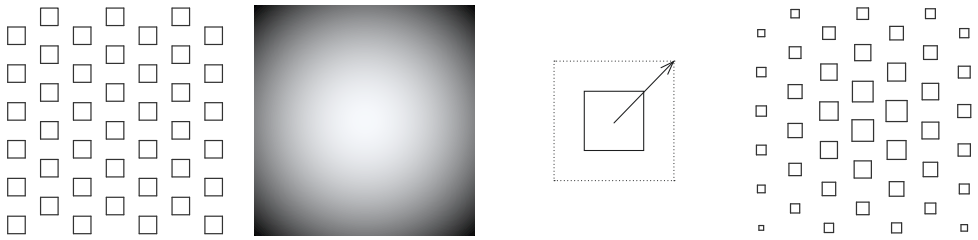

1. INPUT
F : scalar field
(TPMS, lattice, ...)

2. MODIFIER
C : constant
O : operation
F : scalar field
L : plane
V : vector field

3. MODIFIED
T : type
D : dimension
R : ratio
W : wavelength
S : coordinate system

4. OUTPUT
F : scalar field

Figure 2: Graphical overview and nomenclature of the process.

Space frames, spatial lattice structures made of linear bar elements connected in nodes, have long been known for their lightness – or in other terms, their efficient use of only a fraction of material to span across large distances. Instead of by mass per square meter, these structures are often described by their fraction of material per bounding box, i.e. $1-\Phi$, the porosity as defined in Eq. 1. With appropriate strategies for the spatial layout of a space frame's members, this ratio can be as low as 1% [8], or 99% porous in other terms.

Different computational design processes exist to approach this question of optimal material distribution in a given volume, also called the design domain, and topology optimization (TO) is one of them. Even though TO was already introduced over 30 years ago [9] limitations in conventional fabrication methods prevented its wide and direct application. As an alternative to TO, the computational design process can

start from the other end, by specifying the topology and magnitude of internal forces in the members using geometry-based structural form finding methods such as Polyhedral Graphic Statics [10-16]. In this method, the optimal form of the structure for a certain boundary conditions and applied loads are found by geometric construction of force equilibrium. Graphical methods and their various versions in both 2D and 3D have been used extensively by master builders to find efficient structural forms for their design in the past 150 years [17,18].

2.1. Levels of hierarchy

Regardless of what computational design process is used for generating the number, connectivity, dimension and cross section of the bars, the members of the space frame, each one of them can be regarded as a new design domain with certain boundary conditions, namely loads and supports, and serve as the basis for another challenge to determine the most performative porosity. Various levels of optimization can hence be stacked, or recursively nested in a fractal manner. The hull cylinder can again be populated with a polyhedral structure at various levels of subdivision, leading to ever more filigree structures [19,20]. Subsequent levels of porosity design, or optimal material distribution to achieve a target performance can follow different processes and even the use of different materials for core and shell, inspired by bones have been proposed [21]. We choose instead to distribute periodic micro-structures as described in 1.1. and modify their geometry globally and locally according to performance requirements with operations described below.

2.2. Software stack

The initial space frame geometries providing the base elements for this study are developed using the plugin *PolyFrame* [22] for the visual programming environment *Grasshopper* in *Rhino3D* [23]. The geometries for all the samples in this study are generated using the plugin *Axolotl* [24] for *Grasshopper* (see Figure 3). It works with what is called volumetric modelling (VM) based on signed distance functions (SDF) [25]. The field is evaluated at a discrete regular grid interval and an isosurface mesh generated using the marching cubes algorithm [26]. This method has proven more robust than conventional boundary representation modelling (BRep) and is less error prone for Boolean operations even with complex geometries [27]. The resulting meshes are exported in OBJ format and the tetrahedral meshes for the FEA generated using *Wildmeshing* [28]. The FEA finally is performed using *PolyFEM* [29-31]. The results are discussed in Section 3.2.

Figure 3: Palette of the Axolotl plugin in Grasshopper for Rhino.

2.3. Sample geometries

The workflow of modifying specific parameters of one or multiple input fields, by either constants, other scalar fields or vector fields (see Figure 2) can be applied to any geometry. In this study, we focus on TPMS as input and use them to illustrate the effects of modifications and to generate the sample geometries. The different types of modifications, what they modify, and their effect are described below.

1. **Type of TPMS**: A large variety of different TPMS have been found, named and described in literature (Schwartz P (Figure 4e, bottom), Gyroid (Figure 4a-d, e top, g), Diamond (Figure 4f), Neovius, FischerKoch, Lidinoid, IWP etc.). They are all defined as combinations (sums and products) of trigonometric functions with different wavelengths. The function for the simplest, Schwartz P as an example is

$$f(x,y,z) = cos(x) + cos(y) + cos(z) \tag{2}$$

and the minimal surface is wherever this equation returns zero.
Notation: *(F)(C)(T)(F)*

2. **Orientation**: With a matrix transformation applied to the query point *P* at position *(x,y,z)* prior to evaluating the equation, the base plane (origin and orientation in space) of the TPMS structure can be modified.
   Notation: *(F)(L)(S)(F)*
3. **Global wavelength**: The wavelength, the distance after which the pattern periodically repeats (i.e. size of the unit cell) can be modified by multiplying x, y and z by the according factor. This can be done with a uniform value or non-uniform with different values for the different axes.
   Notation: *(F)(C,(C_X,C_Y,C_Z))(W)(F)*
4. **Local wavelength**: Instead of modifying the wavelength globally with constant values, it can also be modified locally by the values of a spatial field. Figure 4c shows the wavelength of a Gyroid modified by the distance to a cylinder placed along the top right edge.
   Notation: *(F)(F)(W)(F)*
5. **Thickness overlay**: By adding a value to the result of the TPMS equation, the geometry can be dilated (negative value) or eroded (positive value) as this shifts the position of the 0-level isocontour. As with the wavelength, this can either be done globally or locally with a field. Figure 4d shows the thickness of a Gyroid modified by the distance to a cylinder placed along the top right edge. A field-driven, locally adaptive thickening result d_R is obtained with

$$d_R = d_A + f * d_B \tag{3}$$

   where d_A is the unmodified distance of the object to be modified (the TPMS), d_B is the distance of the modifier and f is a factor of intensity. Wherever d_B evaluates to zero, the original object A is left unaltered, where d_B is positive, A is eroded, and where d_B is negative, A is dilated.
   Notation: *(F_A)(F_B)(D)(F)*
6. **Shelling**: The minimum surfaces of TPMS separate a volume into equal halves of solid and void. With shelling, the surface itself is given a solid thickness, thereafter separating a volume into two interwoven but unconnected voids, shown in Figure 4g. If $f(x,y,z)=d_A$, where f is the TPMS function and d_A the resulting "distance" of the SDF (note: not metric), then a shell d_R of thickness t can be obtained with

$$d_R = |d_A| - \frac{t}{2} \tag{4}$$

   The values of the various TPMS formulae are not metric distances. For the Schwartz P surface (Eq. 2), they are in the range *[-3,3]*, for a Gyroid in the range *[-1.5,1.5]* and for a Diamond in the range $[-\sqrt{2}, \sqrt{2}]$. The correct value for t in Eq. 4 to obtain a porosity of $\Phi=0.5$ thus has to be found empirically, for the Gyroid it is $t \cong 1.53$, independent of the wavelength.
   Notation: *(F)(O,T)(D)(F)*
7. **Coordinate system**: The periodicity of the structure can consist of unit cell cubes in Cartesian coordinates (Figure 4a), radial "wedges" in a polar coordinate system (Figure 4b), spherical or even following arbitrary local orientations as described later in 2.5.
   Notation: *(F)(V)(S)(F)*
8. **Twist**: Modifications can also be applied to the base coordinate system itself, e.g. rotate the direction of its X-axis around the Z-axis and the rotation angle specified with respect to the distance to the base plane, thus introducing a twist into the object.

$$\theta = z * \alpha$$
$$x' = x * cos(\theta) - y * sin(\theta) \tag{5}$$

$$y' = x * sin(\theta) + y * cos(\theta)$$
$$d = f(x', y', z)$$

where α is the desired rotation angle in radians per distance unit and *(x,y,z)* are the coordinates of the query point. This modification can be used to generate bio-inspired Bouligand structures, that are more flaw-tolerant through damage delocalization [32,33].
Notation: *(F)(C)(S)(F)*

9. **Morph**: As the final shape, the visible geometry, is only a rendering of the zero level iso-contour of a continuous scalar field, multiple fields can be mixed together in any ratio. The morph component combines two input fields and returns a global mix using the following formula:

$$d_R = (1 - f) * d_A + f * d_B \quad (6)$$

where $f \in [0,1]$ is a constant specifying at what ratio to mix the two input fields. If $f=0$ then $d_R=d_A$, if $f=1$ then $d_R=d_B$ and every other value between returns a mix of both inputs.
Notation: $(F_A,F_B)(C)(R)(F_R)$

10. **Blend**: As the final shape, the visible geometry, is only a rendering of the zero level iso-contour of a continuous scalar field, multiple fields can be mixed together in any ratio. The morph component combines two input fields and returns a global mix using the following formula:

$$f = \frac{d_C}{r} + 0.5 \quad (7)$$
$$d_R = (1 - f) * d_A + f * d_B$$

where the factor f is first calculated from the modifier field d_C and and a range r (length of the ramp). The resulting object d_R is hence a blend from d_A to d_B along d_C. Instead of a linear transition, any easing function (quadratic, cubic, trigonometric etc.) can be chosen.
Notation: $(F_A,F_B)(F_C)(R)(F_R)$

We generate a series of cylindrical specimens with the following dimension (in compliance with standard compression test protocols): *ø=150mm, h=300mm* with a volume of $5.3dm^3$. TPMS are based on trigonometric functions and therefore, like a sine wave that has half the curve above and half the curve below the abscissa, non-modified TPMS equations result in a negative value for half the points and in positive values for the other half, the minimal surface thereby separating space in two equal volumes of solid and void. Changing orientation, coordinate system or wavelength (locally or globally) does not affect the porosity. All modified derivatives are hence adjusted to also have a porosity of 0.5 (a solid volume of $2.65dm^3$). For thickening and shelling, the addends have to be adjusted so that as much volume is subtracted in some parts as is added elsewhere.

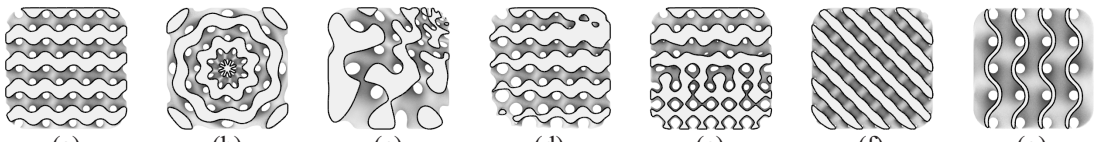

Figure 4: Modifications to the base TPMS: (a) regular Gyroid; (b) polar coordinates; (c) adaptive wavelength; (d) adaptive thickness; (e) transition between types (Schwartz P at the bottom, Gyroid at the top); (f) different type (diamond); and (g) shell.

Any field, resulting from a SDF or other, can act as a modifier for volumetric objects. In Figure 4c and d, the SDF of a cylinder is used to change the thickness or the wavelength of the TPMS respectively. Such a field is shown in Figure 5b where the distance values evaluated in the three unit-planes are shown as colour gradient values ranging from red (negative, inside) over yellow (close to zero, close to the

surface) to blue (positive, outside). The linear blend between two different types of TPMS in Figure 4c is using a plane as modifier (shown in Figure 5a), the field in Figure 5e would result in an output oscillating between the two types.

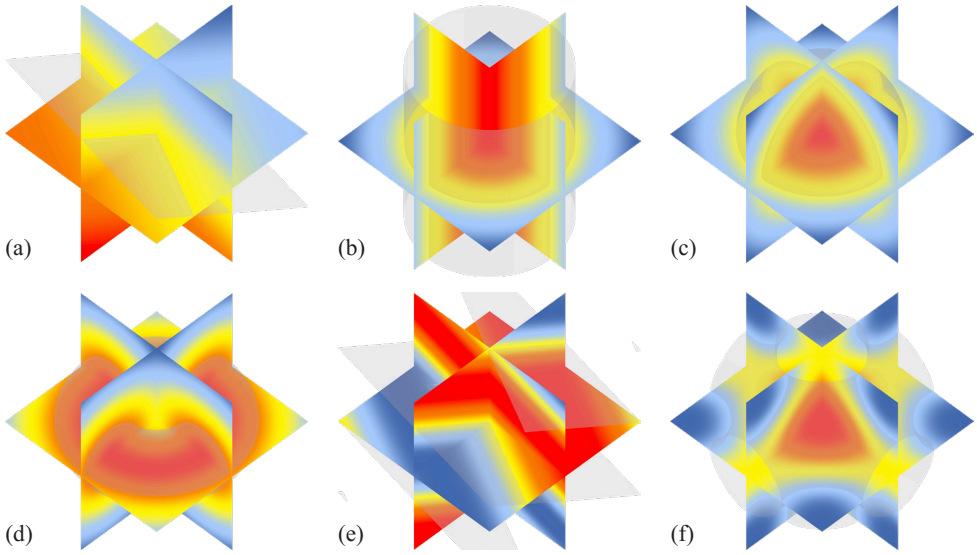

Figure 5: Gradient visualization of distance fields for different primitive geometries, evaluated in the three unit-planes, isosurface of object shown in semi-transparent grey: (a) oblique plane; (b) cylinder; (c) sphere; (d) oblique sinewave; (e) torus; and (f) Schwartz P unit cell (TPMS).

2.4. Field design

Besides simple sums and differences as in Eq. 3 and 4, more advanced mathematical operations can be obtained for complex objects as the combination of primitive input objects. Shapes are thereby computed, rather than constructed. With VM, the final shapes are the result of combining primitives into more complex objects through Boolean operations and other modifications in a constructive solid geometry (CSG) tree. Likewise, the modifying fields are not constrained to be simple primitives but can become the result of an arbitrarily complex CSG tree.

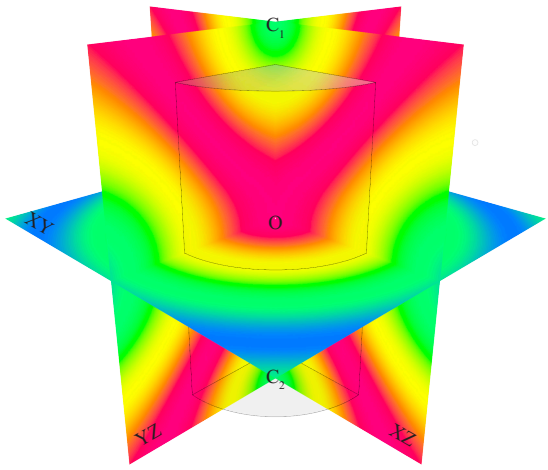

Figure 6: Synthetic distance field used to modify the lattices; test cylinder in grey, field values shown in three planes XY, YZ and XZ.

The synthetic field d_R in Figure 6 shows the typical X-shape of concentrated force distributions in a solid compression test cylinder is obtained by

$$d_R = \frac{d_A - d_B}{d_A + d_B} \tag{8}$$

where d_A is the distance function of a torus in the XY plane centred at the origin (O) and d_B denotes the smooth union of two spheres centred on the Z axis above (C_1) and below (C_2) the cylinder respectively. This particular field is crafted to represent the stress distribution in a compression cylinder. In a future development, the results of the FEA will be directly fed into the modification of the fields.

2.5. Local coordinate system

In chapter 2.3, we describe the use of three basic coordinate systems – Cartesian, polar and spherical – that are applied globally. But like the thickness or the wavelength of a TPMS, also its coordinate system can be differentiated locally. For each point evaluated on the discrete grid, we need a frame describing the rotation at this point in space. This frame is constructed from an origin (the evaluated point) and two perpendicular vectors. To obtain a vector that describes the local orientation of a field, we can use a property of distance fields that they are mostly continuous. We are thereby not interested in the specific distance value, but in the direction of greatest rate of change, the gradient of the distance function *f*. We calculate this by the central difference method shown in Eq. 9 below.

$$\nabla f(x,y,z) = \boldsymbol{v} \begin{bmatrix} f(x-\epsilon,y,z) + f(x+\epsilon,y,z) \\ f(x,y-\epsilon,z) + f(x,y+\epsilon,z) \\ f(x,y,z-\epsilon) + f(x,y,z+\epsilon) \end{bmatrix} \tag{9}$$

where ϵ is a small number (e.g. 0.01) that is big enough to capture the local direction of the gradient at point *(x,y,z)*, but small enough to not catch changes in direction through under-sampling.

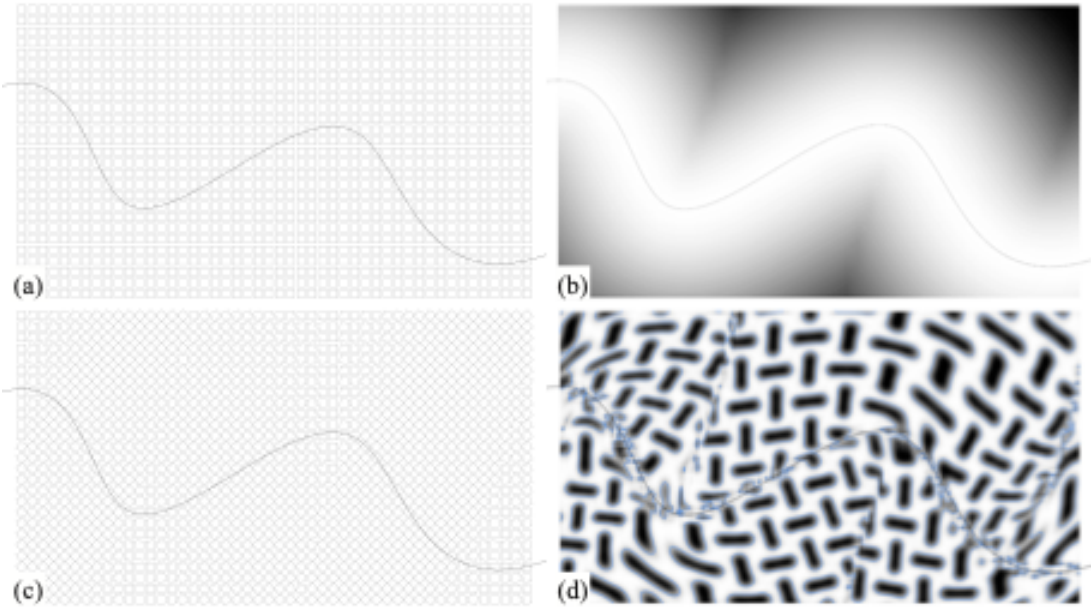

Figure 7: Lattice distortion with local coordinate system based on gradient of distance function.

The steps in which this affects a TPMS (or any other periodic lattice) is shown in Figure 7, illustrated in two dimensions for readability. The starting point is a regular Cartesian coordinate system with the

unit cells periodically repeating along all three axes (Figure 7a). Next, we need a field as a modifier, in the example the distance to the curve (Figure 7b) and the gradient vector $\boldsymbol{v}$ for each individual query point *P*. With this vector, we construct a frame at each point with a specific rotation (Figure 7c). It is important to note, that the squares in Figure 7c do not represent unit cells of the TPMS, but unit planes of the local coordinate system instead. The wavelength of the original undeformed TPMS is ± 7 times bigger than the distance between the query points. A matrix transformation describing the base change from the unit XY plane to the local coordinate system is then applied to the query point, prior to evaluating the TPMS function. The resulting locally distorted TPMS is shown in Figure 7d. The blue lines show the actual surface (zero-level iso-contour), the gray-scale gradient shows the scalar field values.

The resulting modified TPMS in Figure 7d shows some discontinuities of the pattern at the inside of concave parts of the curve. These singularity problems occur at the medial axis, i.e. on ridges in the field that are equidistant to two separate parts of the curve. A possible solution as proposed by [34] is to blur the scalar field first by running a convolution with a Gaussian kernel over it. This will return a new value as a weighted average of the neighbouring field values. Similar artefacts can be observed along the curve, where the gradient vectors' directions do not change smoothly but have opposite directions on either side of the curve. For TPMS lattice types with axial symmetries, this can be addressed by constraining the rotation angle of the local coordinate system to π (axial symmetry) or even $\pi/2$ (rotational symmetry).

Some TPMS can resist more compression in one direction than in another. Schwartz P for example has continuous "struts" parallel to the axes X, Y and Z and may therefore withstand axis-aligned forces better, while other TPMS do not contain continuous straight lines but can better absorb multidirectional forces. Through an orientation modification, the change of basis of the coordinate system, the TPMS can also be turned into a specific direction as shown in Figure 9c. Once a preferable orientation of the chosen lattice is identified, its local coordinate systems can be aligned with the principal stress directions. These stresses can stem from an FEA, be the result of a topology optimization or from the magnitudes of the forces in a 3D graphic statics model. In either case, they have the form of a scalar field, and the vector field of gradient directions can be obtained with the same formula (Eq. 9).

3. Results

The work we present here is in progress, still in its beginning and will be reported upon in future publications. The result of the described method is a computational design workflow. It allows us to generate a large variety of shapes and calculate their mechanical performance through finite element analysis. With all the parameters that can vary, and most of the described modifications can also be combined, there is a high-dimensional and on most axes continuous solution space.

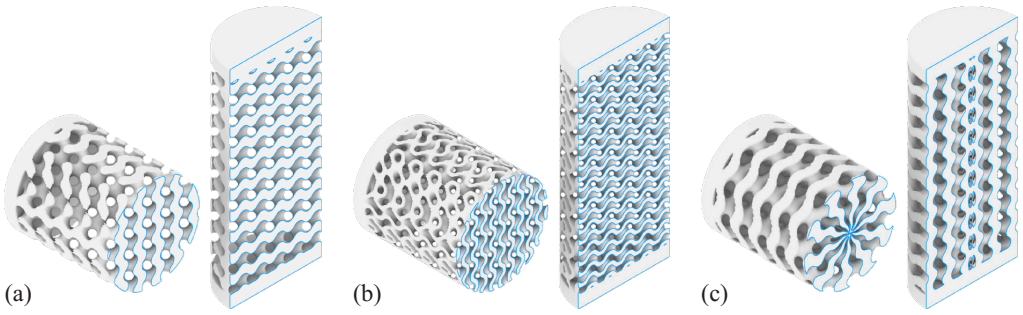

Figure 8: Test cylinders cut along the central planes XY and XZ: (a) regular Gyroid in Cartesian coordinates; (b) shell of the same Gyroid with equal volume; and (c) Gyroid in polar coordinate system.

In Section 2.3, we present a selection of 10 possible modifications. Even if all of them could only take a discrete set of *7* different values (as illustrated for the wavelength on the X-axis in Figure 11, this would result in 7^{10} or over *282* million different geometries. This is a purely theoretical number, many of the modifications don't qualify to be combined or even cancel each other out.

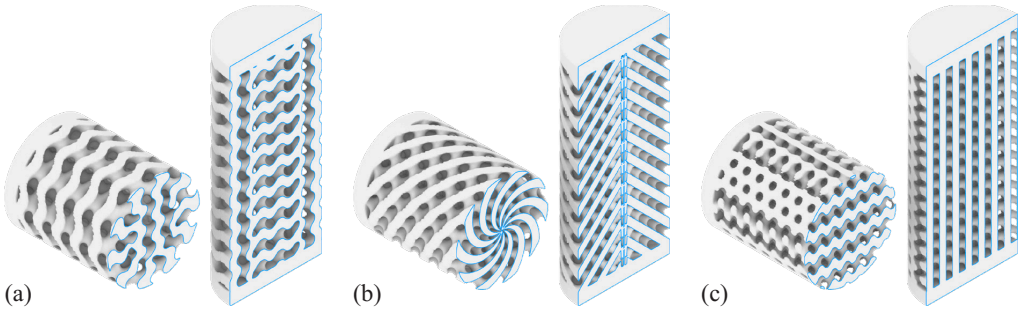

Figure 9: Test cylinders cut along the central planes XY and XZ: (a) blend between Gyroids in a Cartesian (centre) and a polar (periphery) coordinate system; (b) Diamond TPMS in polar coordinates; and (c) regular Diamond with its base rotated to a plane with $\boldsymbol{n}=(0,-1,1)$.

Figure 8a shows that the regular periodicity along all three axes in a Cartesian coordinate system is not optimal for an application in a circular shape, as the Boolean intersection cuts through the lattice pattern at very different angles, causing many different boundary conditions along the contour. A switch to a polar coordinate system homogenizes the boundary of the cylinder as shown in Figure 8c. However, it can also be seen that in the centre the thickness of the solid parts goes down to *0*. These thin shell geometries can on the one hand cause problems with the virtual tetrahedralization for the FEA and on the other hand become a physical problem once these geometries are fabricated, as each material and manufacturing process has certain resolution constraints to be considered. One possible modification to address this issue is to use a blend operation, combining a Cartesian coordinate system at the centre and a polar coordinate system along the periphery, using the distance of another cylinder field (see Figure 5b) as a ramp modifier. The result of this operation is shown in Figure 8a.

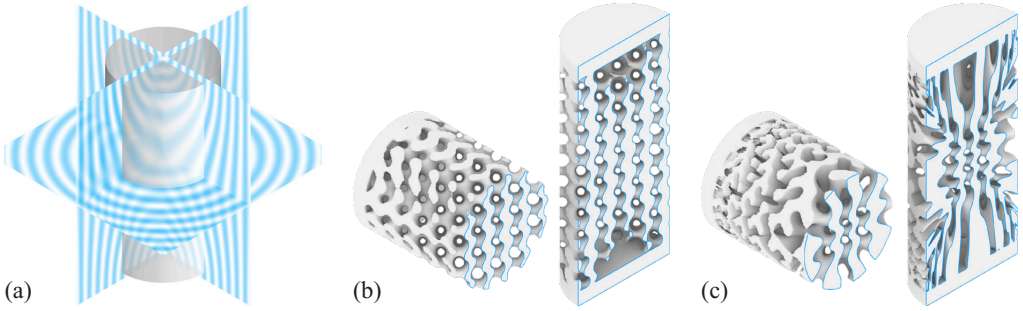

Figure 10: Test cylinders locally modified by a scalar field: (a) visualization of isoparametric regions of the field in the three unit planes; (b) Gyroid with locally modified thickness; and (c) Gyroid with locally modified wavelength.

The six examples presented in Figure 8 and Figure 9 use global modifiers that affect the entire TPMS lattice evenly. They certainly have a different performance when exposed to forces. But what we are really interested in is to use principal stress fields as modifiers to adjust the lattice locally. The field used for the adaptations is shown in Figure 10a (see also Section 2.4. for details). Two exemplary modifications are applied to the regular Gyroid (Figure 8a). In the first (Figure 10b) the thickness of a

regular Gyroid is dilated in regions with high and eroded in regions with low stresses. In the second (Figure 10c) the wavelength of a Gyroid is adjusted locally to smaller unit cells in regions with high stress concentrations. The modifier field can further be used to change other parameters and thereby alter different properties, or its gradient can be extracted to locally align the lattice.

3.1. Grid search

From the plethora of possible modifications, we first identify a subset of 4-5 (M). For each of them, a meaningful domain of parameter values is specified and sampled at N discrete intervals. From the N^M solutions, some can be discarded already based on geometric features, as they contain e.g. degenerate meshes or disjoint parts. The remaining sparse grid is computationally more efficient to run a detailed FE analysis. It is possible to perform the search for best performing parameter configurations hierarchically, from coarse to fine. Once regions with better performing constellations are identified, the corresponding region can be sampled at a finer interval.

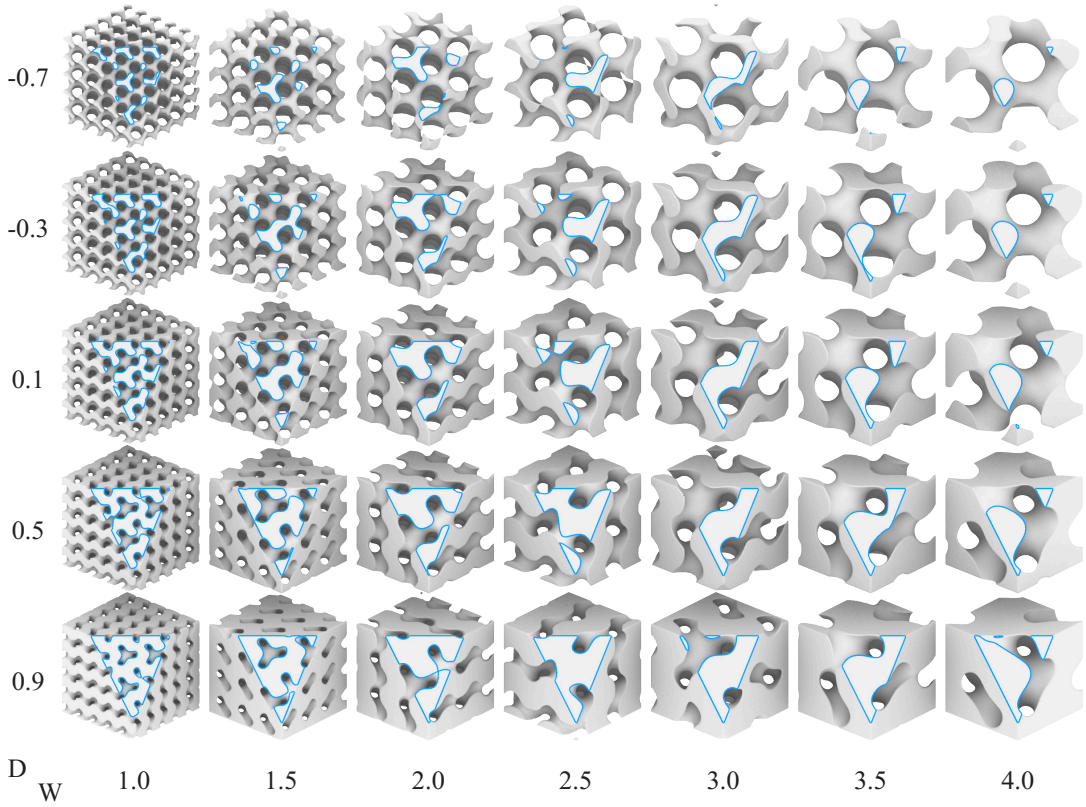

Figure 11: 7x5 samples for a grid search; on the X-axis the wavelength W varies from *1.0* to *4.0*, on the Y-axis the thickness offset D varies from *-0.7* to *0.9*.

3.2. Performance measurement

A simple linear elastic analysis has been performed on the specimens using *PolyFEM*. Results showed that adaptive thickness (Figure 10b) and shell (Figure 8b) specimens have the maximum and minimum deformation of a single node among all the specimens, respectively. In the same category, regular Gyroid, polar Gyroid and polar Diamond specimens have shown almost similar deformation patterns. This is only a preliminary analysis with the need for a more comprehensive modelling to investigate the

performance of each specimen. Therefore, three main criteria (stiffness, strength, and ductility) in evaluating the performance of specimens will be studied. Each specimen's response to the applied loads (axial load here) will define its strength by limiting stresses in individual elements by deforming thereby dissipating energy through the development of internal forces. Therefore, the ability of segments in each specimen and the structure as a whole to undergo deformation while maintaining resistance to loads will be investigated as a measure of energy absorption that considers all the aforementioned criteria. For doing so, a detailed finite element analysis of all specimens will be modelled by applying axial load and measuring the stress distribution along with the height of specimens. Additionally, in order to consider the effect of local failure on each specimen a buckling analysis needs to be performed in future works.

4. Conclusion

We present a suite of computational design instruments that allows the designer to generate, modify, refine and also test lattice infill structures. While the computational design instruments presented in this research are not bound to any scale, their application in architectural elements (e.g. beams, slabs or columns) and an integration of the specific opportunities and constraints of their manufacturing process is the main focus for future development. The packages are freely available and embedded in a CAD environment used by many architects and engineers. This brings advanced light-weighting strategies, formerly only available to specialists and other industries, to the hands of architects and designers. In the present study, we uniquely focus on mechanical properties as performance criteria. The demonstrated workflow using input fields and modifiers to tune specific performance properties however is generic and not limited to neither TPMS as input, nor to principal stresses as modifying fields, nor to structural integrity as the performance criterion. Other criteria could be to design the void V_v instead of the solid part V_s to optimize for the possibility of infrastructure integration or acoustical performance such as reflection and absorption. Once the geometries are materialized as architectural elements, the manufacturing processes inevitably leave visible traces. It is therefore important that architects have instruments at hand that allow to consciously design with these by offering options, rather than having to rely on the single best solution resulting from some black-box optimization.

Acknowledgements

This research was funded by National Science Foundation CAREER Award to Masoud Akbarzadeh (NSF CAREER-1944691 CMMI).

References

[1] L. R. Meza, S. Das, and J. R. Greer, “Strong, lightweight, and recoverable three-dimensional ceramic nanolattices,” *Science*, vol. 345, pp. 1322 LP – 1326, 9 2014.

[2] P. Fratzl and R. Weinkamer, “Nature’s hierarchical materials,” *Progress in Materials Science*, vol. 52, no. 8, pp. 1263–1334, 2007.

[3] A. H. Schoen, “Infinite Periodic Minimal Surfaces without Self-Intersections,” tech. rep., Electronics Research Center, Cambridge, Massachusetts, 5 1970.

[4] D. Barba, E. Alabort, and R. Reed, “Synthetic bone: Design by additive manufacturing,” *Acta Biomaterialia*, vol. 97, pp. 637–656, 2019.

[5] E. C. Clough, T. A. Plaisted, Z. C. Eckel, K. Cante, J. M. Hundley, and T. A. Schaedler, “Elastomeric Microlattice Impact Attenuators,” *Matter*, vol. 1, pp. 1519–1531, dec 2019.

[6] W. Li, G. Yu, and Z. Yu, “Bioinspired heat exchangers based on triply periodic minimal surfaces for supercritical co2 cycles,” *Applied Thermal Engineering*, vol. 179, p. 115686, 2020.

[7] S. Catchpole-Smith, R. Se´lo, A. Davis, I. Ashcroft, C. Tuck, and A. Clare, "Thermal conductivity of tpms lattice structures manufactured via laser powder bed fusion," *Additive Manufacturing*, vol. 30, p. 100846, 09 2019.

[8] M. Akbarzadeh, A. T. Ghomi, M. Bolhassani, M. Akbari, A. S. Ahmadian, K. Papalexiou, J. Sun, and H. Yao, "Saltatur the Dancer," 2020.

[9] M. P. Bendsøe and N. Kikuchi, "Generating Optimal Topologies in Structural Design Using a Homogenisation Method," *Computer Methods in Applied Mechanics and Engineering*, vol. 71, no. 2, p. 197–224, 1988.

[10] M. Akbarzadeh, T. Van Mele, and P. Block, "On the equilibrium of funicular polyhedral frames and convex polyhedral force diagrams," *CAD Computer Aided Design*, vol. 63, pp. 118–128, 2015.

[11] M. Akbarzadeh, *Three Dimensional Graphical Statics using Polyhedral Reciprocal Diagrams.* PhD thesis, ETH Zurich, 2016.

[12] M. Akbarzadeh, T. Van Mele, and P. Block, "Three-dimensional graphic statics: Initial explorations with polyhedral form and force diagrams," *International Journal of Space Structures*, vol. 31, no. 2- 4, pp. 217–226, 2016.

[13] J. Lee, *Computational Design Framework for 3D Graphic Statics.* PhD thesis, Zurich, 2018.

[14] J. Lee, T. Van Mele, and P. Block, "Disjointed force polyhedra," *Computer-Aided Design*, vol. 99, pp. 11–28, June 2018.

[15] A. McRobie, "Maxwell and Rankine reciprocal diagrams via Minkowski sums for 2D and 3D trusses under load," *International Journal of Space Structures*, vol. 31, pp. 115–134, 2016.

[16] A. McRobie, "The geometry of structural equilibrium," *R. Soc. open sci*., vol. 4, no. 160759, 2017.

[17] E. Allen and W. Zalewski, *Form and forces: designing efficient, expressive structures.* John Wiley & Sons, 2009.

[18] W. Zalewski and E. Allen, *Shaping Structures: statics.* New York: Wiley, 1998.

[19] A. T. Ghomi, M. Bolhassani, A. Nejur, and M. Akbarzadeh, "Effect of Subdivision of Force Diagrams on the Local Buckling, Load-Path and Material Use of Founded Forms," in *Proceedings of IASS Annual Symposia*, vol. 2018, pp. 1–8, International Association for Shell and Spatial Structures (IASS), 2018.

[20] M. Bolhassani, A. T. Ghomi, A. Nejur, M. O. Furkan, I. Bartoli, and M. Akbarzadeh, "Structural behavior of a cast-in-place funicular polyhedral concrete: Applied 3D graphic statics," in *Proceedings of IASS Annual Symposia*, vol. 2018, pp. 1–8, International Association for Shell and Spatial Structures (IASS), 2018.

[21] O. Al-Ketan, A. Soliman, A. M. AlQubaisi, and R. K. Abu Al-Rub, "Nature-Inspired Lightweight Cellular Co-Continuous Composites with Architected Periodic Gyroidal Structures," *Advanced Engineering Materials*, vol. 37, p. 1700549, 10 2017.

[22] M. Akbarzadeh and A. Nejur, "PolyFrame for Rhino Manual," tech. rep., PSL UPenn, Philadelphia, PA, 2018.

[23] D. Rutten, "Grasshopper," 2007.

[24] M. Bernhard, "Axolotl," 2018. *www.food4rhino.com/app/axolotl*

[25] M. Bernhard, M. Hansmeyer, and B. Dillenburger, "Volumetric modelling for 3D printed architecture," in *AAG - Advances in Architectural Geometry* (L. Hesselgren, A. Kilian, O. Sorkine Hornung, S. Malek, K.-G. Olsson, and C. J. K. Williams, eds.), (Göteborg, Sweden), pp. 392–415, Klein Publishing GmbH, 2018.

[26] W. E. Lorensen and H. E. Cline, "Marching cubes: A high resolution 3D surface construction algorithm," *Proceedings of the 14th annual conference on Computer graphics and interactive techniques* - SIGGRAPH '87, vol. 21, no. 4, pp. 163–169, 1987.

[27] McNeel, "Why Booleans Fail," 2000.

[28] Y. Hu, Q. Zhou, X. Gao, A. Jacobson, D. Zorin, and D. Panozzo, "Tetrahedral meshing in the wild," *ACM Transactions on Graphics*, vol. 37, no. 4, pp. 1–18, 2018.

[29] T. Schneider, J. Dumas, X. Gao, M. Botsch, D. Panozzo, and D. Zorin, "Poly-Spline Finite-Element Method," *ACM Trans. Graph.*, vol. 38, 3 2019.

[30] T. Schneider, Y. Hu, J. Dumas, X. Gao, D. Panozzo, and D. Zorin, "Decoupling Simulation Accuracy from Mesh Quality," *ACM Transactions on Graphics*, vol. 37, no. 6, 2018.

[31] T. Schneider, Y. Hu, J. Dumas, X. Gao, D. Panozzo, and D. Zorin, "Decoupling simulation accuracy from mesh quality," SIGGRAPH Asia 2018 Technical Papers, vol. 37, no. 6, 2018.

[32] V. R. Sherman, H. Quan, W. Yang, R. O. Ritchie, and M. A. Meyers, "A comparative study of piscine defense: The scales of Arapaima gigas, Latimeria chalumnae and Atractosteus spatula," *Journal of the Mechanical Behavior of Biomedical Materials*, vol. 73, no. May 2016, pp. 1–16, 2017.

[33] M. Moini, J. Olek, J. P. Youngblood, B. Magee, and P. D. Zavattieri, "Additive Manufacturing and Performance of Architectured Cement-Based Materials," *Advanced Materials*, vol. 30, no. 43, 2018.

[34] A. Schmeißer, R. Wegener, D. Hietel, and H. Hagen, "Smooth convolution-based distance functions," *Graphical Models*, vol. 82, pp. 67–76, 2015.